Title

CD8+ T-Cell Density Imaging with 64Cu-Labeled Cys-Diabody Informs Immunotherapy Protocols

Journal

Clinical Cancer Research, 24(20)

ISSN

1078-0432

Authors

Seo, Jai Woong
Tavaré, Richard
Mahakian, Lisa M
et al.

Publication Date

2018-10-15

DOI

10.1158/1078-0432.ccr-18-0261

Peer reviewed

HHS Public Access

Author manuscript

Clin Cancer Res. Author manuscript; available in PMC 2019 October 15.

Published in final edited form as:

Clin Cancer Res. 2018 October 15; 24(20): 4976–4987. doi:10.1158/1078-0432.CCR-18-0261.

CD8+ T-cell density imaging with ^{64}Cu-labeled cys-diabody informs immunotherapy protocols

Jai Woong Seo[1], **Richard Tavaré**[2], **Lisa M. Mahakian**[1], **Matthew T. Silvestrini**[1], **Sarah Tam**[1], **Elizabeth S. Ingham**[1], **Felix B. Salazar**[2], **Alexander D. Borowsky**[3], **Anna M. Wu**[2,^], and **Katherine W. Ferrara**[1,*,^]

[1]Department of Biomedical Engineering, University of California, Davis, CA, 95616

[2]Crump Institute for Molecular Imaging, Department of Molecular and Medical Pharmacology, David Geffen School of Medicine, University of California, Los Angeles, CA 90095

[3]Center for Comparative Medicine, University of California, Davis, CA, 95616

Abstract

Purpose—Noninvasive and quantitative tracking of CD8$^+$ T-cells by positron emission tomography (PET) has emerged as a potential technique to gauge response to immunotherapy. We apply an anti-CD8 cys-diabody, labeled with ^{64}Cu, to assess the sensitivity of PET imaging of normal and diseased tissue.

Experimental Design—Radiolabeling of an anti-CD8 cys-diabody (169cDb) with ^{64}Cu was developed. The accumulation of ^{64}Cu-169cDb was evaluated with PET/CT imaging (0, 5, and 24 hours) and biodistribution (24 hours) in wild-type mouse strains (n = 8 per group studied with imaging and immunohistochemistry or flow cytometry) after intravenous administration. Tumor-infiltrating CD8$^+$ T-cells in tumor bearing mice treated with CpG and αPD-1 were quantified and mapped (n = 6–8 per group studied with imaging and immunohistochemistry or flow cytometry).

Results—We demonstrate the ability of immunoPET to detect small differences in CD8$^+$ T-cell distribution between mouse strains and across lymphoid tissues, including the intestinal tract of normal mice. In FVB mice bearing a syngeneic *HER2*-driven model of mammary adenocarcinoma (NDL), ^{64}Cu-169cDb PET imaging accurately visualized and quantified changes in tumor-infiltrating CD8$^+$ T-cells in response to immunotherapy. A reduction in the circulation time of the imaging probe followed the development of treatment-related liver and splenic hypertrophy and provided an indication of off-target effects associated with immunotherapy protocols.

*To whom correspondence should be addressed: Prof. Katherine W. Ferrara, Dept. of Biomedical Engineering, 451 Health Sciences Drive, University of California, Davis, Davis, CA 95616, PHONE 530-754-9436, FAX (530) 754-5739, kwferrara@ucdavis.edu.
^These authors contributed equally to this work.

The authors declare no potential conflicts of interest.

J.W.S. designed and conducted experiments, performed the analysis and wrote the manuscript; E.S.I. and M.T.S. designed and conducted experiments and performed analysis; L.M.M. and S.M.T. maintained mouse models, provided assistance with design and conduct of experiments. F.B.S and R.T. developed and produced the diabody and contributed to the experimental design, A.B. performed immunohistochemistry, K.W.F. and A.M.W. planned and initiated the project, designed experiments, wrote the manuscript and supervised the project.

Conclusion—^{64}Cu-169cDb imaging can spatially map the distribution of CD8^{+} T-cells in normal organs and tumors. ImmunoPET imaging of tumor-infiltrating cytotoxic CD8^{+} T-cells detected changes in T-cell density resulting from adjuvant and checkpoint immunotherapy protocols in our pre-clinical evaluation.

Introduction

Immune responses are complex, involving multiple organs and tissues, and featuring a spectrum of cell types, including the innate and adaptive arms of the immune system. Current approaches for monitoring immune responses are powerful yet limited (1,2). For example, blood cells and biomarkers can provide a wealth of information on immune status and responses, using techniques such as highly multiplexed flow cytometry, genomic/transcriptomic/proteomic profiling of immune cell subsets, and equally sophisticated assessment of soluble biomarkers (cytokines and other serum markers, circulating DNA, exosomes, etc.). However, analysis of blood and serum markers provides little specific information regarding spatial localization and interaction of key immune effector cells *in situ*. Instead, tissues obtained from limited clinical biopsies, or at necropsy in preclinical models, provide materials for analysis. In contrast, sensitive, non-invasive molecular imaging techniques such as positron emission tomography (PET) can provide the required specificity to distinguish immune system components in living organisms over the course of disease development and progression, and during therapies that trigger immune responses (3,4).

Checkpoint inhibitors are particularly promising components of current therapeutic strategies for cancer treatment (5–7). Monotherapeutic clinical trials with immune checkpoint inhibitors, such as anti-programmed cell death protein-1 (αPD-1), anti-programed death-ligand1 (αPD-L1), and anti-cytotoxic T-lymphocyte-associate protein 4 (αCTLA-4) have shown objective response rates from 5% to 60% in various solid cancers (8–11). Other immune checkpoints (e.g. TIM3, PD-L2, BTLA, LAG-3, TIGIT) (12) and many co-stimulatory checkpoint molecules (e.g. ICOS, ICOSL, OX40, 4-1BB, CD27, CD28) have been discovered and are being developed as new drugs (13). Patient response remains limited in tumors lacking a robust T-cell infiltrate, and strategies to enhance the T-cell density are under evaluation (14). Multiple strategies to enhance response have been proposed, including additional systemic chemotherapies (15–17) or immunotherapies (18,19) and focal therapies such as radiation or ablation (20–25). Pre-clinical models suggest that generating a robust anti-tumor innate immune activation may be necessary to overcome tumor-mediated immune suppression. In particular, toll-like receptor activation yields increased antigen retention and results in more effective induction of CD8^{+} T-cell responses (26). In preclinical animal studies, combining checkpoint inhibitors with toll-like receptor 9 (TLR9) agonists, such as CpG-oligodeoxynucleotides (CpG-ODN), enhanced the therapeutic response (27,28).

Given the many emerging therapeutic options, non-invasive differentiation between responders and non-responders in early treatment is important. Simply monitoring tumor size is a poor early-indicator of response; efficacious therapy may increase tumor diameter due to enhancement of the tumor immune-infiltrate. An ideal monitoring technique for

patients receiving immunotherapy would measure the immune response itself, and $CD8^+$ T-cells are of particular interest. The presence of tumor-infiltrating $CD8^+$ T-cells has in fact been suggested as a prognostic tool in colon cancer (29), non-small cell lung cancer (NSCLC), (30), ovarian cancer (31,32), and melanoma (33). ImmunoPET, which combines the specificity of antibodies with the imaging advantages of PET, is therefore an attractive option. PET imaging of $CD8^+$ T-cells in a murine model (34) has been accomplished using a ^{64}Cu radiolabeled minibody (Mb, 80 kDa) engineered to selectively bind to $CD8^+$ T-cells. In addition, lymphoid organs have been visualized using a cys-diabody (cDb, 55 kDa) labeled with ^{89}Zr ($t_{1/2}$ = 78.4 h) and engineered for renal (rather than liver) clearance (35). With the ^{89}Zr-malDFO-169cDb imaging probe, preclinical imaging detected intratumoral $CD8^+$ T-cell responses to checkpoint immunotherapy (36). Other investigations have recently suggested PD-1 expression on $CD8^+$ T-cells as a prognostic biomarker in pancreatic ductal adenocarcinoma and imaging techniques to map T-cell markers are in development (37). Monitoring $CD8^+$ T-cell density and phenotype is possible by biopsy, but biopsies cannot map the spatial heterogeneity or detect changes in localization of $CD8^+$ T-cells with time. PET imaging strategies can also inform biopsy by guiding tissue sampling to regions of enhanced or reduced T-cell density.

Here, we radiolabeled a 169cDb probe, which specifically targets $CD8^+$ T-cells, with ^{64}Cu ($t_{1/2}$ = 12.7 h) and applied PET to image and quantify the $CD8^+$ T-cell population in living subjects. Specifically, we sought to determine the accuracy and sensitivity of PET imaging in mapping of the normal endogenous T-cell distribution within various tissues, in quantification of the variability in T-cell distribution between subjects, in the detection of treatment-related hypertrophy associated with immunotherapy protocols, and in spatially mapping T-cell density over the course of immunotherapy.

Materials and Methods

$^{64}CuCl_2$ was purchased from Washington University School of Medicine (MIR Cyclotron Facility). Metal-free ammonium citrate and sodium hydroxide were purchased from Sigma-Aldrich and prepared as a solution in double distilled water. Centrifugal spin columns were purchased from Bio-Rad (Bio-Spin® 6, MWCO <6 kD). Dulbecco's phosphate-buffered saline (DPBS,1X) without calcium and magnesium was purchased from Thermo Fisher Scientific. CpG oligonucleotide 1826 was purchased from InvivoGen (San Diego, CA) and anti-PD-1 (αPD-1) monoclonal antibody was purchased from BioXCell (clone RMP1-14, Lebanon, NH).

Modification of 169cDb

The modification of 169cDb followed a previously reported procedure (36). In brief, 169cDb (100–165 μg, MW: 54.1 kDa, 3.0–4.0 mg/mL) was diluted in DPBS (50 μL) and 0.1 M tris(2-carboxyethyl)phosphine (TCEP, 10 equiv. of 169cDb, pH 7.0) in DPBS was added to the 169cDb solution in order to reduce disulfide bonds. Afterwards, the reaction was kept at room temperature for 30 min. TETA-maleimide (756.84 g/mol) in DPBS (5 equiv. of 169cDb, 1 μg/μL) was then added to the mixture and incubated for 2 h at room temperature. The reaction mixture was filtered through a spin column (1000 x g, 4 min.) filled with 0.1 M

ammonium citrate (pH 7.5). The collected solution was finally eluted via gravity filtration through the spin column filled with 0.1 M ammonium citrate (pH 7.5) to achieve complete buffer exchange. UV absorbance of each collected fraction (0.1 mL/fraction) was measured at 254 and 280 nm to measure the concentration of TETA-169cDb.

^{64}Cu-labeling of TETA-169cDb

All radiolabeling experiments were conducted under a radiation use authorization (RUA) approved by the University of California, Davis. $^{64}CuCl_2$ (82–144 kBq) in diluted 0.1 M HCl was added to a solution of TETA-169cDb (67–104 μg) in 0.1 M ammonium citrate buffer (pH 7.5, 0.1 mL). The pH was adjusted to 6 with 1 M NaOH and kept at room temperature for 30 min. Reaction progress was monitored by instant thin layer chromatography (ITLC) with a 0.1 M ammonium citrate eluent (pH 5.5). Following the addition of 0.1 M EDTA (10 μL), the reaction mixture was kept at room temperature for an additional 10 min and filtered through a spin column (1000 x g, 4 min) filled with DPBS. The filtered solution was then eluted via gravity filtration through the spin column. The early fraction with the highest radioactivity was diluted with DPBS to prepare the final dose concentration. The diluted solution was sterilized with a 0.2 μm filter. Radiochemical purity was determined with ITLC.

Protein gel electrophoresis

169cDb, TETA-169cDb, and ^{64}Cu-169cDb were loaded into a 20 μL volume with Tris-Glycine SDS buffer and run on a 14% Tris-Glycine gel in an electrophoresis chamber filled with Tris-Glycine SDS buffer under 220V for 40 min. The gel was washed with double distilled water and protein bands were stained with SafeStain (Invitrogen). The gel was exposed on a Storage Phosphor Screen (Molecular Dynamics, CA) for 6 h, and analyzed on a Storm 860 Imaging System (Amersham Bio-Science, NJ).

Size exclusion chromatography analysis of 169cDb, TETA-169cDb, and ^{64}Cu-169cDb

169cDb, TETA-169cDb, and ^{64}Cu-169cDb were analyzed by HPLC connected to a size exclusion column (MWCO 1kDa-300kDa, 300x7.8 mm) in a 1 mg/mL flow rate. UV absorbance and radioactivity were detected at 280 nm and with a flow-counter, respectively.

Animal models

Studies with Imaging—All animal experiments were conducted under an animal use protocol approved by the University of California, Davis, Institutional Animal Care and Use Committee (IACUC). The ^{64}Cu-169cDb evaluation in wild-type FVB, BALB/c, and C57BL/6 mice included 4–5 week old female BALB/c mice (n=4), 4–5 week old female C57BL/6 mice (n=4) (The Jackson laboratory, Bar Harbor, ME), and 4–5 week old female FVB/n mice (n=8: n=4 *in vivo*, n=4 *ex vivo* only as described in the supplement) (Charles River, Wilmington, MA).

For ^{64}Cu-169cDb evaluation in tumor-bearing FVB mice, FVB/n mice (n=18) (Charles River, Wilmington, MA) were orthotopically transplanted with syngeneic NDL tumor biopsies (~1 mm^3) bilaterally into the #4 and #9 inguinal mammary fat pads as previously described (38). Tumor sizes were monitored with ultrasound twice a week. Once tumors

reached approximately 0.5 cm in the largest tumor diameter (~3 weeks post-transplantation), mice were randomized into groups including multiple-treatment (MT), single-treatments (ST) and non-treatment controls (NT). For MT (CpG+αPD-1) mice (n=4), CpG was injected into a single tumor on days 27, 30 and 34 post tumor implantation and αPD-1 was injected on days 27 and 34 followed by PET at day 36. ST studies included a single dose each of CpG+αPD-1 (n=4 mice), CpG only (n=3) or αPD-1 only (n=3) on day 30 post tumor implant followed by PET on day 36. For all groups, αPD-1 was injected intraperitoneally (IP) (200 μg in 50 μl) and CpG was injected intratumorally (IT) (100 μg in 50 μL) into a single tumor. NT control mice (n=4) received no immunotherapy treatment. Tumor diameters were measured weekly with standard ultrasound (Siemens Sequoia 512, Issaquah, WA).

Studies with flow cytometry

From wild-type mice (FVB and BALB/c): axillary (n=2 nodes per mouse), inguinal (n=2 nodes per mouse), or cervical (n=2 nodes per mouse) lymph nodes were harvested from 6-week old wild-type FVB (n=4) and BALB/c (n=4) mice. Flow cytometric analysis of immune cell populations in lymph nodes was performed when all wild-type mice were 6 weeks old.

From FVB mice bearing tumors: Bilateral NDL-tumor mice (n=11) received a single injection of anti-PD-1 (ST αPD-1, n=4) or CpG+αPD-1(ST CpG+αPD-1, n=4) on day 30 post tumor transplantation, or no treatment (NT, n=3). For all relevant groups, anti-PD-1 mAb was injected intraperitoneally (i.p.) at a dose of 200 μg and CpG was injected intratumorally (i.t.) into a single tumor at a dose of 100 μg. Flow cytometric analysis of immune cell populations in tumors, inguinal lymph nodes and spleen was performed on day 37 post tumor transplantation, as described in the supplementary methods.

PET/CT scans and biodistribution

Mice were anesthetized with 3.0% isoflurane in oxygen and maintained under 1.5–2.0% isoflurane. ^{64}Cu-169cDb (4.15 ± 1.11 μg/animal, 6.78 ± 1.22 MBq/animal) was administered by tail vein injection and PET imaging was conducted on an Inveon DPET small animal PET scanner (Siemens Medical Solutions USA, Knoxville, TN) for 30 min at 0, 5 and 24 h post injection. After each PET scan, the animals were moved to a small animal Inveon MM CT system (Siemens Medical Solutions USA, Knoxville, TN) and a CT scan was conducted to obtain anatomical information for co-registration of PET/CT images. Whole body activity was measured between scans with a gamma-counter (Capintec, Inc. NJ). After the final imaging time point, mice were euthanized by cervical dislocation under deep isoflurane. Blood, urine and organs (thymus, bone, stomach, intestine, liver, spleen, kidneys, heart, lungs, thigh muscle), lymph nodes (inguinal, axillary, mesenteric, cervical), and tumors were harvested for biodistribution analysis using a 1470 automatic gamma counter (PerkinElmer, CT) after which organs weights were taken on a microbalance. In some cases, organs were briefly scanned to obtain *ex-vivo* PET data and organs were evaluated with histological stains.

Region of interest analysis and time–activity curves

All PET images were reconstructed with the maximum a posteriori (MAP) reconstruction algorithm and analyzed with AsiPro software (Siemens Medical Solutions Inc., USA) and Inveon Research Workspace 4.2 (Siemens Medical Solutions Inc., USA). Regions of interest (ROIs) of bilateral tumors and blood were drawn after the co-registration of PET/CT images. To obtain the time-activity curve (TAC) of blood, blood radioactivity at 0 (30 min segmented to 6 frames), 5, and 24 h were fitted with one-phase decay curve with Prism 6 for Mac OS. Radioactivity density was presented as percent injected dose per cubic centimeter (%ID/cc)

Histology

Tissues for microscopic analysis were fixed overnight in 10% buffered formalin and transferred to 70% ethanol the next day. A Tissue-Tek VIP autoprocessor (Sakura, Torrance, CA) was used to process samples for paraffin-embedding. Tissue blocks were sectioned to 4 μm sections and were mounted on glass slides. Samples were then stained with hematoxylin and eosin (H&E) or were processed for immunohistochemistry (IHC) using a rat anti-mouse CD8a primary antibody (1:500; 14-0808, eBiosciences) or goat anti-mouse PECAM-1 (CD31) primary antibody (1:1600; SC-1506, Santa Cruz Biotechnology, Santa Cruz, CA). All IHC was performed manually without the use of an automated immunostainer. Antigen retrieval was performed using a Decloaking Chamber (Biocare Medical, Concord, CA) with citrate buffer at pH 6.0, 125 degrees C and pressure to 15 psi. The total time slides were in the chamber was 45 min. Incubation with the primary antibody was performed at room temperature overnight in a humidified chamber. Normal goat or horse serum were used for blocking. Biotinylated goat anti-rat (CD8a) (1:500; Vector Labs, Burlingame, CA) and biotinylated horse anti-goat (CD31) (1:1000; Vector Labs, Burlingame, CA) were the secondary antibodies used with a Vectastain ABC Kit Elite and a Peroxidase Substrate Kit DAB (both from Vector Labs) used for amplification and visualization of signal, respectively. Stained slides were scanned on an AT2 Scanscope (Leica Biosystems) and digital images viewed using the Imagescope program (Leica Biosystems).

Statistical Analysis

Statistical significance was determined with either an unpaired t-test with Welch's correction or an ordinary one-way ANOVA with Tukey's multiple comparison test, which was performed in GraphPad Prism software (Prism 6.0). Statistical significance is presented as $*P \leq 0.05$, $** P \leq 0.01$, $*** P \leq 0.001$, and $**** P \leq 0.0001$.

Results

Labeling and characterization of TETA-169cDb

169cDb was site-specifically modified with TETA-maleimide (Fig. 1*A*) conjugated to cysteine, as previously demonstrated for nanoparticles (39). Following this step, the chelator-to-protein ratio of TETA-169cDb, as calculated from the peak intensity of MALDI mass, was 1.3:1 (Fig. S1). Recovery yield of TETA-169cDb after two *in situ* isolations using a spin column was 74 ± 12%. Incorporation of ^{64}Cu into isolated TETA-169cDb in citrate buffer gave ^{64}Cu-169cDb at a yield of 66 ± 9% (n=4, decay corrected) and a radiochemical

purity of >99% in instant thin-layer chromatography (ITLC). Specific activity of ^{64}Cu-169cDb was 1.77 ± 0.60 MBq/μg at the end of synthesis. SDS-PAGE gel electrophoresis of 169cDb (Fig. 1*B*, lane 1), TETA-169cDb (Fig. 1*B*, lane 2), and ^{64}Cu-169cDb (Fig. 1*B*, lane 3 and 3a) demonstrated that 169cDb was reduced and modified to TETA-169cDb, as shown by the slightly higher molecular weight band of TETA-169cDb (lane 2) compared to that of 169cDb at ~25 kDa (lane 1). Autoradiography showed both monomeric and dimeric forms of ^{64}Cu-169cDb (Fig. 1*B*, lane 3a). The elution profiles (Fig. 1*C*) of 169cDb (top), TETA-169cDb (middle), and ^{64}Cu-169cDb (bottom) from the size exclusion column showed that the divalent diabody was not disrupted after modification and ^{64}Cu labeling.

^{64}Cu-169cDb in wild-type FVB, BALB/c, and C57BL/6 mice depicts strain variation in CD8^{+} T-cell distribution in lymph nodes and gut

CD8^{+} T-cell imaging was first evaluated in FVB, BALB/c, and C57BL/6 mice of similar age and body weight (Table S1) following intravenous injection of 3.72 ± 0.30 μg of ^{64}Cu-169cDb (7.46 ± 0.53 MBq/animal). Projected PET/CT images acquired at 24 h (Fig. 2*A*) showed that ^{64}Cu-169cDb primarily accumulated in the lymphoid organs [lymph nodes (white arrows), spleen (blue capital S)], kidney (blue capital K), and in the small intestine (yellow capital I and arrow) of all three strains. Pharmacokinetic parameters (K value) were largely similar among the strains (Table S2); however, in the lymph nodes (pooled from axillary, inguinal, cervical, and mesenteric lymph nodes), accumulation of ^{64}Cu-169cDb was lower in BALB/c (46.0 ± 13.2 %ID/g) as compared with FVB (68.8 ± 17.3 %ID/g) and C57BL/6 mice (66.0 ± 15.5 %ID/g) (Fig. 2*B*). The differences in the ^{64}Cu-169cDb accumulation as a function of mouse strain were then validated by flow cytometry. The number of T-cells ($5.43\times10^{6} \pm 1.57\times10^{6}$ FVB vs $2.86\times10^{6} \pm 0.95\times10^{6}$ BALB/c, $P = 0.0001$, Fig. 2*C*), the fraction of T-cells as a percentage of live cells (76.7 ± 5.1% FVB vs 69.4 ± 3.4% BALB/c, $P = 0.0006$, Fig. 2*D*) and the number of CD8^{+} T cells ($1.51\times10^{6} \pm 0.42\times10^{6}$ FVB vs $0.87\times10^{6} \pm 0.30\times10^{6}$ BALB/c, $P = 0.0004$, Fig. 2*E*) in the pooled nodes were all significantly greater in the FVB as compared with the BALB/c strain. The ratio of diabody accumulation in the FVB vs BALB/c strains assessed with PET was similar to the ratio of the number of CD8^{+} T cells quantified by flow cytometry (FVB ~1.5 fold higher than BALB/c in both assays). Further, two reasons for the enhanced accumulation of the diabody in the FVB mice were evident. First, the FVB lymph nodes were larger (5.89 ± 1.07 mg FVB vs 4.96 ± 1.72 mg BALB/c) and contained a greater number of leukocytes ($6.2\times10^{6} \pm 1.8\times10^{6}$ FVB vs $3.6\times10^{6} \pm 1.1\times10^{6}$ BALB/c, $P = 0.0005$). Second, T-cells constituted a larger fraction of the leukocytes in the FVB lymph nodes (87% of the leukocytes).

At 24 h after injection, accumulation of ^{64}Cu-169cDb in the proximal intestinal tract (adjacent to the stomach) was also clearly visualized in the 3D-rotational image of the whole mouse (Video S1). *Ex vivo* PET images of the intestines from FVB mice, acquired after cleaning the intestine lumen, confirmed an intestinal accumulation of ^{64}Cu-169cDb (Fig. S2*A*, Method *S2*). Quantification of radioactivity in specific sections of the intestinal tract using a well counter demonstrated the highest accumulation of ^{64}Cu-169cDb in the duodenum (nearly 10 %ID/g) and a gradual decrease from the jejunum to the ileum (~3.5 %ID/g) (Fig. S2*B*). Radioactivity in both the intestine and in the feces were similar at

5 (5.14 ± 1.20 %ID/g) and 24 (6.07 ± 0.39 %ID/g) hours. Radioactivity is excreted in the feces but also accumulates within the intestinal tract. In an additional study (Table S3), we did not clear the intestines of feces, but in either case, the distribution of accumulation was very similar, and the presence of the discrete foci represented by the feces did not preclude imaging of the distribution of T-cells. In the study without clearing intestinal contents, 24 h accumulation in C57BL/6 mice was, for example, ~14 %ID/g in the duodenum decreasing to ~6 %ID/g in the ileum (Table S3).

Results of immunotherapy in NDL tumor-bearing FVB mice

Previously, we investigated tumor infiltration of $CD8^+$ T-cells in FVB mice bearing the syngeneic orthotropic *neu* exon deletion line (NDL) model of breast cancer (40,41). We found that seven days of immunotherapy with a TLR9 agonist (CpG-ODN, CpG) and checkpoint inhibitor (anti-PD-1: αPD-1) increased the number of $CD8^+$ T-cells in tumors of the CpG+αPD-1-treated group (42,43). In the present study, we followed a multiple-treatment protocol (MT) of CpG+αPD-1 adapted from our previous tumor-priming studies (42,43), a single-treatment protocol (ST) of CpG+αPD-1, CpG, or αPD-1, and a control protocol (no-treatment cohort, NT) as indicated in Fig. 3*A*. In FVB mice bearing bilateral tumors transplanted in the fourth and ninth mammary fat pads, CpG was injected intratumorally into one of the two tumors and αPD-1 was injected intraperitoneally. Tumor size and average body weight in the five experimental groups are summarized in Fig. 3*B* and Table S4–S5. At day 34 post transplantation, all treatments significantly reduced growth compared to the non-treated control. The treated tumors ranged in volume from 0.296 to 0.011 cm^3 and had a mean volume of 0.076 ± 0.049 cm^3. The mean weight of the MT tumors was the smallest among all groups and was significantly smaller than the NT and ST (αPD-1) cohorts (Fig. 3*C*). Upon hematoxylin and eosin (H&E) staining, the MT protocol resulted in a significant reduction in viable tumor, with extensive necrosis and loss of cell-cell integrity within the lesions. Particularly within the MT-treated tumors, an extensive inflammatory reaction surrounded the lesion (Fig. S3). Necrosis was also evident in the directly-treated and distant tumors following the ST (CpG+αPD-1) protocol, and in the directly-treated ST (CpG) tumors.

Single immunotherapy treatments enhance T-cell density and enhancement is imaged with ^{64}Cu-169cDb

$CD8^+$ T-cell imaging of NDL tumor-bearing mice after immunotherapy was performed by systemic administration of ^{64}Cu-169cDb (i.v. injection, 4.44 ± 1.35 μg/animal, 6.33 ± 1.34 MBq/animal). The ^{64}Cu-169cDb distribution in FVB mice with bilateral NDL tumors was then assessed for the various treatments. Compared with NT and MT mice (Fig. 4*A, B*), tumor accumulation of ^{64}Cu-169cDb was enhanced on PET/CT slice images (yellow arrows) in ST mice (Fig. 4*C–E*) at both 5 and 24 h. Radioactivity was greatest in the rim of all tumors and was greater in the rim of ST tumors (Fig. 4*C–E*, **bottom transverse images**) compared to NT and MT tumors (Fig. 4*A*, *B*, **bottom transverse images**), especially at 24 h. $CD8^+$ T-cells were observed in the tumors of MT mice; however, a significant fraction of the MT tumors was necrotic, without apparent functional vasculature (Fig. S3).

Radioactivity of tumors excised at 24 h was greater in ST mice (CpG+αPD-1: 3.91 ± 0.64 %ID/g, CpG: 3.51 ± 1.08 %ID/g, and αPD-1: 4.54 ± 0.32 %ID/g) than in NT mice (2.43 ± 0.51 %ID/g) and MT mice (1.75 ± 0.60 %ID/g) (Fig. 4*F* and Table S7). Thus, the accumulation of the probe increased 1.4 to 1.9-fold in the ST mice compared to the NT mice. We compared the imaging results to estimates of changes in $CD8^+$ T-cells obtained by flow cytometry (Fig. 4G). Within the tumor, $CD8^+$ T-cells as a fraction of $CD45^+$ cells were 5.1, 9.5 and 15.1% in the NT, αPD-1 and CpG+αPD-1-treated groups and therefore increased by 1.9 and 3-fold compared to non-treated tumors, respectively (Fig. 4G). When $CD8^+$ T-cells were estimated as a fraction of live cells, the increase was 1.7 and 4.6-fold for αPD-1 and CpG+αPD-1-treated tumors, respectively, as compared with the NT control (data not shown).

At the time of injection, radioactivity (%ID/g and SUV) in the MT and ST (CpG+αPD-1) groups was reduced as compared with the NT group, likely resulting from a reduced blood volume within these treated tumors (Fig. S4*A, D*). Results from ROI image analysis of tumors at 5 and 24 h after ^{64}Cu-169cDb injection (Fig. S4*B–C, E–F*) were similar to the biodistribution of ^{64}Cu-169cDb in the tumor at 24 h (Fig. 4*F*). As a function of time, radioactivity increased between 0 and 5 h in all treatment groups and decreased between 5 and 24 h (Fig. 4*H*). Although not significant, the accumulation of radioactivity in tumors receiving a direct CpG injection was slightly lower than that in the non-injected contralateral tumor of each treated animal (Fig. S5).

A comparison of the PET images with CD8a immunohistochemistry (IHC) from the MT tumors confirmed the ability of PET imaging to spatially map the regions of necrosis and viable tumor with ongoing $CD8^+$ T-cell infiltration (Fig. 5). Regions of viable tumor T-cell infiltration and with dimensions on the order of 2 mm correspond to regions in the IHC in both the contralateral and CpG-injected tumors. H&E staining of tumors from NT and ST (αPD-1) mice indicate a greater blood volume as compared to tumors treated with CpG (Fig. S6, **upper row**). Additionally, CD31 staining of tumor vasculature also validated the greater endothelial surface area within tumors from NT mice and ST (αPD-1) mice (Fig. S6, **middle row**). In agreement with the observed tumor accumulation of the ^{64}Cu-169cDb probe, immunohistochemistry (IHC) using a $CD8^+$ T-cell staining antibody in tumor tissue confirmed the enhanced infiltration of $CD8^+$ T-cells in the tumors of ST mice compared to those of NT mice (Fig. S6, **lower row**). IHC indicated a greater density of infiltrating $CD8^+$ T-cells (arrows) near blood vessels in the tumors from MT and ST mice than in NT mice (Fig. S6, **lower row**).

Treatment with CpG affects ^{64}Cu-169cDb distribution and pharmacokinetics in lymph nodes, spleen, and liver of NDL tumor-bearing mice

The pharmacokinetics were then assessed through projection imaging, where ^{64}Cu-169cDb accumulation in the lymph nodes (white arrows), liver (blue capital L) and spleen (blue capital S) was apparent (Fig. 6*A–E*). Most importantly, accumulation of the ^{64}Cu-169cDb was evident in the lymph nodes (Fig. 6*A–E*, **white arrow**). High intestinal radioactivity (indicated by capital I and yellow arrows) was observed in NT (Fig. 6*A*) and ST mice (Fig. 6*C–E*) but not in MT mice (Fig. 6*B*). Pharmacokinetic (PK) parameters from blood ROI

analysis (Table S6 and Fig. 6*F*, K value, half-life, and AUC) showed that the blood clearance of ^{64}Cu-169cDb was increased for the MT group ($t_{1/2}$ = 41.3 min, k = 0.0168 min^{-1}) as compared to the NT ($t_{1/2}$ = 63.3 min, k = 0.0111 min^{-1}) and ST groups (which include 1: CpG+αPD-1 ($t_{1/2}$ = 59.7 min, k = 0.0116 min^{-1}), 2: CpG ($t_{1/2}$ = 82.2 min, k = 0.0084 min^{-1}), and 3: αPD-1 ($t_{1/2}$ = 66.7 min, k = 0.0104 min^{-1})). Slightly higher blood radioactivity in MT mice was observed at 24 h (Fig. 6*G*, Table S7). As compared to NT and ST mice, PET/CT projection images of MT mice acquired at 5 h after ^{64}Cu-169cDb administration (left images in all frames) showed a higher intensity in the liver (white capital L) (Fig. 6*A*–*E*).

The differences in liver and spleen radioactivity resulted at least in part from treatment-related hypertrophy (Fig. S7*A*–*K*). Changes in the spleen morphology as a function of the treatment groups were evident on optical imaging (Fig. S7*A*–*E*) and were confirmed by the *ex vivo* weight (Fig. S7*F*). For the MT cohort, the spleens were 2.4-fold heavier compared to the NT group ($p < 0.01$) (Fig. S7*F*), and the splenic volume of ST mice (Fig. S7*C*–*E*, *F*) was similar to the NT group. Total accumulation (%ID) in the spleen at 24 h did not differ significantly among the groups (Fig. S7*G*). Radioactive density (%ID/g) was enhanced in the spleen of ST mice (CpG+αPD-1: 27.58 ± 2.49 %ID/g, $p < 0.0001$ and αPD-1: 39.52 ± 5.37 %ID/g, $p < 0.01$) as compared to the NT mice (19.37 ± 4.55 %ID/g, $p < 0.05$), confirming the higher splenic image intensity observed in these mice at 24 hours. Splenic radioactive density was reduced in the MT mice (9.28 ± 1.94 %ID/g) as compared to the NT group and single treatments incorporating αPD-1 (Fig. S7*H*, Table S7).

The livers of MT mice were also 1.95-fold heavier (2.76 ± 0.38 g) as compared to the livers (1.41 ± 0.10 g) from NT mice ($p < 0.01$) (Fig. S7*I*). Even a single treatment of CpG+αPD-1 resulted in an increased average liver weight relative to NT mice (Fig. S7*I*). The resulting total accumulation (%ID) of radioactivity in the liver was greatly enhanced in the MT group, and was enhanced in the ST (CpG+αPD-1) and ST (CpG) groups, each as compared with the NT cohort (Fig. S7*J*). Radioactive density (%ID/g) was enhanced in the liver of ST (αPD-1) mice as compared to the NT group, with a general, but not significant, trend toward enhanced density across the treated groups (Fig. S7*K*, Table S7).

The impact of treatment was also evident in liver and spleen histopathology (Fig. S8). In the MT cohort, extensive extramedullary hematopoiesis and perivascular accumulation of granulocytes were evident upon liver H&E staining (Fig. S8*A*, top rows). CD8^{+} T-cells infiltrated in greater numbers near liver veins and sinusoids in MT mice as compared to liver tissue from NT mice (Fig. S8*A*, bottom row). The spleens from MT mice contained larger areas of red and white pulp (Fig. S8*B*, top rows). Splenic CD8a staining (Fig. S8*B*, bottom row) showed more CD8^{+} cells in the periarterial lymphatic sheaths of MT mice than those in the NT mice. H&E and CD8a staining of liver and spleen from MT and NT mice were also examined to determine whether treatment-related remodeling of the liver and spleen was independent of the administration of the imaging probe. H&E images obtained from the liver and spleen of NT mice after the administration of 169cDb confirmed that the hepatosplenomegaly did not result from 169cDb but rather from the acute effect of intratumoral injection of CpG (data not shown).

Lymph nodes in the MT mice were also enlarged (Fig. S7*L*). The total accumulation in lymph nodes from ST mice was enhanced as compared with the NT and MT mice (Fig. S7*M*), and the mean density was greater in the ST, as compared with the NT and MT, mice (Fig. S7*N*).

Tracking radioactivity within the intestines

We also investigated the intestinal radioactivity that was observed in the projected PET/CT images (Fig. 6*A*–*E*). The lower accumulation of ^{64}Cu-169cDb in the intestine of MT mice was confirmed by the organ distribution of radioactivity (Fig. S9). As we previously observed in the intestines of wild-type mice (Fig. S2), ^{64}Cu-169cDb radioactivity in all groups was the highest in the duodenum and gradually decreased from the jejunum to the colon.

Conclusions/Discussion

Here, we successfully developed ^{64}Cu-169cDb as an immunoPET imaging agent targeting CD8$^+$ T-cells. Previously, studies of immunoPET using monoclonal antibodies used positron emitters, such as I-124 (100.2 h) and Zr-89 (78.4 h), which have relatively long half-lives because of the extended blood residual time of mAbs. In comparison, 169cDb engineered from an anti-CD8 antibody circulates for a period of hours in the blood (36). Thus, we developed a labeling method for 169cDb using ^{64}Cu ($t_{1/2}$ = 12.7 h). The use of ^{64}Cu reduces radiation exposure compared to ^{89}Zr-DFO and the $t_{1/2}$ (12.7 h) of ^{64}Cu was also more suitable than shorter-lived PET isotopes (^{18}F or ^{68}Ga). The chelator-to-protein ratio of TETA-169cDb (1.3:1 in our study) was similar to the dye-to-protein ratio (1.5:1) previously achieved with a maleimide-fluorescent dye (36). After labeling with ^{64}Cu, ^{64}Cu-TETA-169cDb retained the CD8$^+$ binding shown in (36) with ^{89}Zr-169cDb. The radiochemical purity of ^{64}Cu-169cDb (>99%) was comparable to that of ^{89}Zr-169cDb.

We then demonstrated that immunoPET imaging after systemic administration of ^{64}Cu-169cDb can be used to 1) detect differences in CD8$^+$ T-cell distribution across normal subjects and in tumor-infiltrating CD8$^+$ T-cells within a murine model of breast cancer receiving immunotherapy; 2) map the distribution of CD8$^+$ T-cells within normal tissues such as the intestine; and 3) visualize the effects of multi-dose immunotherapy on diabody circulation and tumor viability. Most importantly, this new imaging probe facilitates serial imaging of T-cell distribution over the course of treatment. We compared results acquired following single or multiple treatments with immunotherapy and found that immunoPET can be combined with anatomical imaging to map viable tumor and regions of T-cell infiltration. We previously applied a similar immunotherapy strategy to that used here in (42) and demonstrated enhanced survival was associated with the enhanced CD8$^+$ T-cell infiltration. We have now shown that the imaging strategy accurately quantified the enhanced infiltration.

This technology could in the future be applied to assess CD8$^+$ T-cell infiltration as a function of time and treatment. Biopsy could potentially be directed to regions with enhanced infiltration to further probe the immunocyte populations. In both pre-clinical and clinical

studies, the baseline T-cell infiltration can vary widely; therefore, the ability to non-invasively assess density before and during treatment is important (14,42).

In addition to the strategy described here, multiple probes are under development for imaging $CD8^+$ T-cell activation, including probes for IFNγ (44) and Granzyme B (45). Imaging of T-cell activation is of great interest; however, there are advantages to imaging the infiltration of T-cells (instead of or in addition to imaging of activation). First, in our pre-clinical work, we find that the increase in infiltrating T-cells can be quite large with a successful immunotherapy protocol and therefore can provide a sensitive and potentially early biomarker for the success of an immunotherapy regimen. Further, in flow cytometry assays of CpG and αPD-1 therapy (43), the fraction of cells producing IFNγ at a single time point is small (a few percent) and therefore the sensitivity of a probe of activation may be lower. Second, activation of specific markers can be short lived following a specific immunotherapy regimen and therefore the timing of probes for T-cell activation may require optimization for an individual treatment protocol. Therefore, the imaging of infiltration could provide a useful surrogate. In addition, PET imaging strategies that allow for the imaging of multiple targets are also under development and may facilitate imaging of both infiltration and activation in the future. Dual-tracer PET/CT imaging is advancing with new detector and processing capabilities facilitating simultaneous imaging acquisition from multiple targets (46). A lower dose of radioactivity can be used with total body PET scanners and may allow serial PET scans of infiltrating $CD8^+$ T-cells and activation markers (47).

Sensitivity and specificity of the imaging strategy

We evaluated the pharmacokinetics of ^{64}Cu-169cDb in multiple mouse strains (FVB, BALB/c, and C57BL/6), and found that the blood clearance of the probe was similar (Fig. S10). The blood radioactivity we observed was also similar to that previously observed in wild-type AKR mice at 22 h after administration of ^{89}Zr-malDFO-169cDb (36), indicating that the stability of ^{64}Cu-169cDb is comparable to ^{89}Zr-malDFO-169cDb. The accumulation of the ^{64}Cu-169cDb in the pooled lymph nodes (47–86 %ID/g) and the spleen (62–81 %ID/g) was greater than that of ^{89}Zr-malDFO-169cDb in all mouse strains studied (lymph nodes: 37–42 %ID/g, spleen: 23 %ID/g). Further, the muscle accumulation of the ^{64}Cu-169cDb diabody was lower in all three strains than that observed with ^{89}Zr-malDFO-169cDb in AKR. Although the lymphatic-to-muscle ratio and detection sensitivity observed here were greater than those reported in the ^{89}Zr-malDFO-169cDb study, the difference in the injected dose (here the dose was lower) precludes a direct comparison of the performance. Blocking studies, included in (36), demonstrated the specificity of the diabody, with a reduction in accumulation in the lymphatic organs and intestine in response to diabody injection.

Using invasive methods, Pinchuk *et al.,* reported that the $CD8^+$ T-cell population in the spleen of C57BL/6 mice was greater than in BALB/c mice (48). We similarly observed a reduced accumulation of ^{64}Cu-169cDb in the spleen, lymph nodes, and intestine of BALB/c mice compared to the other mouse strains tested. We confirmed the differences in $CD8^+$ T

cells between mouse strains using flow cytometry and validated that the ~1.5 ratio in diabody accumulation was indicative of the cell populations.

In humans and mice, the $CD8^+$ lymphocyte population in the gut is highest in the proximal small intestine (49,50). We also observed that intestinal radioactivity (%ID/g at 24 h) decreased from the duodenum to the ileum, which implies that mapping of the T-cell distribution within the intestine is feasible and a ^{64}Cu-169cDb probe could potentially be used to investigate $CD8^+$ related bowel disease (51,52).

Effects of multi-dose immunotherapy on perfusion and tumor viability

Due to the low objective response rate of single checkpoint inhibitor therapy, more recent therapies use combination protocols including multiple chemotherapy or immunotherapy components (53–55), surgical removal and/or ablation of the tumor by radiation (56,57) or ultrasound therapy (42). Here, our immunoPET study sought to quantify tumor infiltrating $CD8^+$ T-cells after single or combination immunotherapy with CpG and αPD-1. CpG triggers an immunomodulatory response that expands $CD8^+$ T-cells (58,59) and αPD-1, an immune check-point inhibitor, increases the frequency of tumor infiltrating $CD8^+$ T-cells (60,61). In our results from CD8 IHC staining of tumors, $CD8^+$ T-cells were more evident in tumors from treated mice than in tumors from NT mice. ^{64}Cu-169cDb accumulation measured by gamma counter and ROI analyses of tumors at 5 and 24 h also demonstrated higher infiltration of $CD8^+$ T-cell populations in tumors from ST mice as compared to NT mice.

H&E and CD31 staining demonstrated necrosis and a reduced vascular volume in all CpG-treated tumors relative to contralateral tumors. Although the accumulation of ^{64}Cu-169cDb between CpG-treated and contralateral tumors was not significantly different, the trend toward a reduced accumulation of ^{64}Cu-169cDb in CpG-treated tumors versus contralateral tumors could also be related to anti-vascularization and the necrosis of the directly-treated tumors observed on H&E. Further, the tumor accumulation of ^{64}Cu-169cDb in ST mice with αPD-1 was higher than in ST mice treated with CpG+αPD-1 ($P < 0.05$). This may result from the longer circulation time of ^{64}Cu-169cDb in ST (αPD-1) mice.

Multiple treatments with CpG+αPD-1 slowed tumor growth and enhanced the IHC estimates of the $CD8^+$ T-cell population in the tumor margin as compared to the NT cohort. The total accumulation of ^{64}Cu-169cDb in the MT group was similar to that of the NT group. The reason for this, we believe, is two-fold. First, multiple treatments with CpG +αPD-1 resulted in extensive tumor necrosis with a decrease in the blood volume within the treated tumors. A reduction in microvessel density (62,63) has been reported previously with such a protocol. Here, we demonstrate that PET imaging can map the regions of necrosis and of enhanced accumulation and this spatial mapping will be critically important in the interpretation of the treatment efficacy. Second, CpG treatment (58,64) caused hypertrophy of the liver and spleen, which reduced the circulation time of ^{64}Cu-169cDb and therefore decreased the potential accumulation in target sites. This is particularly evident in the reduced accumulation within lymph nodes following the MT protocol. In fact, the area under curve (AUC) of the blood activity for MT-treated mice was 68%, 74% and 74 % of AUC of

that for the ST αPD-1, CpG, CpG+αPD-1 treated mice. Due to the combination of the decrease in blood circulation of the probe, the tumor necrosis and the reduction in the vascular volume, the tumor accumulation of ^{64}Cu-169cDb in MT mice was 38%, 49%, and 44% of that observed for ST (αPD-1), (CpG), and (CpG+αPD-1) mice, respectively. Liver hypertrophy and the resulting changes in circulation and accumulation of immunotherapeutic agents have implications for therapeutic efficacy. Changes in the diabody pharmacokinetics resulting from treatment with CpG are likely to be replicated with other immunotherapy-related antibodies. The imaging agent described here has the potential to highlight such changes and thus detect off-target systemic effects. Future human studies of immunotherapy protocols with imaging probes must account for the impact of tumor necrosis and liver hypertrophy when present.

Study limitations

The advantages of imaging methods to track specific immune cell populations include the ability to spatially map the distribution of a specific population and to repeat the study over time. However, using PET, one or at best two populations can be assessed. Other markers of response include multiplexed immunohistochemistry, circulating cytokines, flow cytometry and RNA sequencing of samples obtained from tumor or blood can provide substantial additional information regarding response. Thus, multiple techniques may be required to provide sufficient information to fully assess response. Further, additional imaging studies of alternate immunotherapy protocols are required in order to determine where the CD8^{+} T-cell diabody is best applied.

We conclude that the ^{64}Cu-169cDb has the potential to quantify CD8^{+} T-cell density within and between subjects. This imaging agent can be applied to monitor the effects of immunotherapy on the distribution of T-cells within a therapeutic regimen. Early-stage immunoPET imaging of tumor-infiltrating cytotoxic CD8^{+} T-cells, particularly in combination with imaging of tumor necrosis, may aid in the assessment of efficacy. Our results demonstrate that toxicity inducing a hypertrophy of liver and spleen must be considered in the analysis of immunoPET imaging data. Assessment of liver and spleen hypertrophy on anatomical imaging can inform the interpretation of such data.

Supplementary Material

Refer to Web version on PubMed Central for supplementary material.

Acknowledgments

This project was supported by NIHR01CA210553 (J. Seo, K. Ferrara), NIHR01CA134659 (M. Silvestrini, E. Ingham, S. Tam, L. Mahakian, K. Ferrara) and NIHR01CA199658 (E. Ingham, S. Tam, L. Mahakian, K. Ferrara) and by a pilot grant from the University of California-Davis Center for Molecular and Genomic Imaging (http://bme.ucdavis.edu/cmgi/). A.M.W. is a member of the UCLA Jonsson Comprehensive Cancer Center (NIH P30 CA 016042). The authors appreciate the assistance of Susannah Bloch in the preparation of the manuscript. This project was also supported by the University of California Davis Flow Cytometry Shared Resource Laboratory and with technical assistance from Ms. Bridget McLaughlin and Mr. Jonathan Van Dyke. UC Davis core resources are funded from the NCI P30 CA093373 (Cancer Center), and NIH NCRR C06-RR12088, S10 OD018223, S10 RR12964 and S10 RR 026825 grants.

Abbreviations

CT	computed tomography
TIM3	T-cell immunoglobulin and mucin-domain containing-3
PD-L2	Programmed death ligand 2
BTLA	B- and T-lymphocyte attenuator
LAG-3	lymphocyte activation gene-3
TIGIT	T cell immunoglobulin and ITIM domain
ICOS	inducible T-cell costimulatory
ICOSL	inducible T-cell costimulator ligand
IFNγ	interferon gamma
MALDI	matrix assisted laser desorption/ionization
TETA	1,4,8,11-tetraazacyclotetradecane-N,N′,N″,N‴-tetraacetic acid
EDTA	ethylenediaminetetraacetic acid
MWCO	molecular weight cut-off
DPBS	Dulbecco's phosphate-buffered saline

References

1. Wargo JA, Reddy SM, Reuben A, Sharma P. Monitoring immune responses in the tumor microenvironment. Curr Opin Immunol. 2016; 41:23–31. DOI: 10.1016/j.coi.2016.05.006 [PubMed: 27240055]
2. Furman D, Davis MM. New approaches to understanding the immune response to vaccination and infection. Vaccine. 2015; 33(40):5271–81. DOI: 10.1016/j.vaccine.2015.06.117 [PubMed: 26232539]
3. Laing RE, Nair-Gill E, Witte ON, Radu CG. Visualizing cancer and immune cell function with metabolic positron emission tomography. Curr Opin Genet Dev. 2010; 20(1):100–5. DOI: 10.1016/j.gde.2009.10.008 [PubMed: 19931447]
4. Keu KV, Witney TH, Yaghoubi S, Rosenberg J, Kurien A, Magnusson R, et al. Reporter gene imaging of targeted T cell immunotherapy in recurrent glioma. Sci Transl Med. 2017; 9(373)doi: 10.1126/scitranslmed.aag2196
5. Sharma P, Allison JP. The future of immune checkpoint therapy. Science. 2015; 348(6230):56–61. DOI: 10.1126/science.aaa8172 [PubMed: 25838373]
6. Postow MA, Callahan MK, Wolchok JD. Immune Checkpoint Blockade in Cancer Therapy. J Clin Oncol. 2015; 33(17):1974–82. DOI: 10.1200/JCO.2014.59.4358 [PubMed: 25605845]
7. Pardoll DM. The blockade of immune checkpoints in cancer immunotherapy. Nat Rev Cancer. 2012; 12(4):252–64. DOI: 10.1038/nrc3239 [PubMed: 22437870]
8. Brahmer JR, Tykodi SS, Chow LQ, Hwu WJ, Topalian SL, Hwu P, et al. Safety and activity of anti-PD-L1 antibody in patients with advanced cancer. New Engl J Med. 2012; 366(26):2455–65. DOI: 10.1056/NEJMoa1200694 [PubMed: 22658128]

9. Topalian SL, Hodi FS, Brahmer JR, Gettinger SN, Smith DC, McDermott DF, et al. Safety, activity, and immune correlates of anti-PD-1 antibody in cancer. New Engl J Med. 2012; 366(26):2443–54. DOI: 10.1056/NEJMoa1200690 [PubMed: 22658127]
10. Royal RE, Levy C, Turner K, Mathur A, Hughes M, Kammula US, et al. Phase 2 trial of single agent Ipilimumab (anti-CTLA-4) for locally advanced or metastatic pancreatic adenocarcinoma. J Immunother. 2010; 33(8):828–33. DOI: 10.1097/CJI.0b013e3181eec14c [PubMed: 20842054]
11. Postow MA, Chesney J, Pavlick AC, Robert C, Grossmann K, McDermott D, et al. Nivolumab and ipilimumab versus ipilimumab in untreated melanoma. New Engl J Med. 2015; 372(21):2006–17. DOI: 10.1056/NEJMoa1414428 [PubMed: 25891304]
12. Collin M. Immune checkpoint inhibitors: a patent review (2010–2015). Expert Opin Ther Pat. 2016; 26(5):555–64. DOI: 10.1080/13543776.2016.1176150 [PubMed: 27054314]
13. Dempke WCM, Fenchel K, Uciechowski P, Dale SP. Second- and third-generation drugs for immuno-oncology treatment-The more the better? Eur J Cancer. 2017; 74:55–72. DOI: 10.1016/j.ejca.2017.01.001 [PubMed: 28335888]
14. Gajewski TF. The Next Hurdle in Cancer Immunotherapy: Overcoming the Non-T-Cell-Inflamed Tumor Microenvironment. Semin Oncol. 2015; 42(4):663–71. DOI: 10.1053/j.seminoncol.2015.05.011 [PubMed: 26320069]
15. Nowak AK, Robinson BW, Lake RA. Synergy between chemotherapy and immunotherapy in the treatment of established murine solid tumors. Cancer Res. 2003; 63(15):4490–6. [PubMed: 12907622]
16. Baxevanis CN, Perez SA, Papamichail M. Combinatorial treatments including vaccines, chemotherapy and monoclonal antibodies for cancer therapy. Cancer Immunol Immunother. 2009; 58(3):317–24. DOI: 10.1007/s00262-008-0576-4 [PubMed: 18704409]
17. Steer HJ, Lake RA, Nowak AK, Robinson BW. Harnessing the immune response to treat cancer. Oncogene. 2010; 29(48):6301–13. DOI: 10.1038/onc.2010.437 [PubMed: 20856204]
18. Marabelle A, Kohrt H, Sagiv-Barfi I, Ajami B, Axtell RC, Zhou G, et al. Depleting tumor-specific Tregs at a single site eradicates disseminated tumors. J Clin Invest. 2013; 123(6):2447–63. DOI: 10.1172/JCI64859 [PubMed: 23728179]
19. Davila E, Kennedy R, Celis E. Generation of antitumor immunity by cytotoxic T lymphocyte epitope peptide vaccination, CpG-oligodeoxynucleotide adjuvant, and CTLA-4 blockade. Cancer Res. 2003; 63(12):3281–8. [PubMed: 12810660]
20. Formenti SC, Demaria S. Combining radiotherapy and cancer immunotherapy: a paradigm shift. J Natl Cancer Inst. 2013; 105(4):256–65. DOI: 10.1093/jnci/djs629 [PubMed: 23291374]
21. Dromi SA, Walsh MP, Herby S, Traughber B, Xie J, Sharma KV, et al. Radiofrequency ablation induces antigen-presenting cell infiltration and amplification of weak tumor-induced immunity. Radiology. 2009; 251(1):58–66. DOI: 10.1148/radiol.2511072175 [PubMed: 19251937]
22. Gursel E, Roberts M, Veenema RJ. Regression of prostatic cancer following sequential cryotherapy to the prostate. J Urol. 1972; 108(6):928–32. [PubMed: 4117196]
23. Roach MC, Videtic GMM, Bradley JD, Committee IART. Treatment of Peripheral Non-Small Cell Lung Carcinoma with Stereotactic Body Radiation Therapy. J Thorac Oncol. 2015; 10(9):1261–7. DOI: 10.1097/JTO.0000000000000610 [PubMed: 26291009]
24. Xu Y, Shen Q, Wang N, Wu PP, Huang B, Kuang M, et al. Microwave ablation is as effective as radiofrequency ablation for very-early-stage hepatocellular carcinoma. Chin J Cancer. 2017; 36(1):14.doi: 10.1186/s40880-017-0183-x [PubMed: 28103953]
25. Yu MA, Liang P, Yu XL, Han ZY, Dong XJ, Wang YU, et al. Multiple courses of immunotherapy with different immune cell types for patients with hepatocellular carcinoma after microwave ablation. Exp Ther Med. 2015; 10(4):1460–6. DOI: 10.3892/etm.2015.2681 [PubMed: 26622507]
26. Krieg AM. Toll-like receptor 9 (TLR9) agonists in the treatment of cancer. Oncogene. 2008; 27(2):161–7. DOI: 10.1038/sj.onc.1210911 [PubMed: 18176597]
27. Wang S, Campos J, Gallotta M, Gong M, Crain C, Naik E, et al. Intratumoral injection of a CpG oligonucleotide reverts resistance to PD-1 blockade by expanding multifunctional CD8+ T cells. Proc Natl Acad Sci U S A. 2016; 113(46):E7240–E9. DOI: 10.1073/pnas.1608555113 [PubMed: 27799536]

28. Mangsbo SM, Sandin LC, Anger K, Korman AJ, Loskog A, Totterman TH. Enhanced tumor eradication by combining CTLA-4 or PD-1 blockade with CpG therapy. J Immunother. 2010; 33(3):225–35. DOI: 10.1097/CJI.0b013e3181c01fcb [PubMed: 20445343]
29. Pages F, Kirilovsky A, Mlecnik B, Asslaber M, Tosolini M, Bindea G, et al. In situ cytotoxic and memory T cells predict outcome in patients with early-stage colorectal cancer. J Clin Oncol. 2009; 27(35):5944–51. DOI: 10.1200/JCO.2008.19.6147 [PubMed: 19858404]
30. Kawai O, Ishii G, Kubota K, Murata Y, Naito Y, Mizuno T, et al. Predominant infiltration of macrophages and CD8(+) T Cells in cancer nests is a significant predictor of survival in stage IV nonsmall cell lung cancer. Cancer-Am Cancer Soc. 2008; 113(6):1387–95. DOI: 10.1002/cncr.23712
31. Stumpf M, Hasenburg A, Riener MO, Jutting U, Wang C, Shen Y, et al. Intraepithelial CD8-positive T lymphocytes predict survival for patients with serous stage III ovarian carcinomas: relevance of clonal selection of T lymphocytes. Brit J Cancer. 2009; 101(9):1513–21. DOI: 10.1038/sj.bjc.6605274 [PubMed: 19861998]
32. Sato E, Olson SH, Ahn J, Bundy B, Nishikawa H, Qian F, et al. Intraepithelial CD8+ tumor-infiltrating lymphocytes and a high CD8+/regulatory T cell ratio are associated with favorable prognosis in ovarian cancer. Proc Natl Acad Sci U S A. 2005; 102(51):18538–43. DOI: 10.1073/pnas.0509182102 [PubMed: 16344461]
33. Mullins IM, Slingluff CL, Lee JK, Garbee CF, Shu J, Anderson SG, et al. CXC chemokine receptor 3 expression by activated CD8+ T cells is associated with survival in melanoma patients with stage III disease. Cancer Res. 2004; 64(21):7697–701. DOI: 10.1158/0008-5472.CAN-04-2059 [PubMed: 15520172]
34. Tavare R, McCracken MN, Zettlitz KA, Knowles SM, Salazar FB, Olafsen T, et al. Engineered antibody fragments for immuno-PET imaging of endogenous CD8+ T cells in vivo. Proc Natl Acad Sci U S A. 2014; 111(3):1108–13. DOI: 10.1073/pnas.1316922111 [PubMed: 24390540]
35. Tavare R, McCracken MN, Zettlitz KA, Salazar FB, Olafsen T, Witte ON, et al. Immuno-PET of Murine T Cell Reconstitution Postadoptive Stem Cell Transplantation Using Anti-CD4 and Anti-CD8 Cys-Diabodies. J Nucl Med. 2015; 56(8):1258–64. DOI: 10.2967/jnumed.114.153338 [PubMed: 25952734]
36. Tavare R, Escuin-Ordinas H, Mok S, McCracken MN, Zettlitz KA, Salazar FB, et al. An Effective Immuno-PET Imaging Method to Monitor CD8-Dependent Responses to Immunotherapy. Cancer Res. 2016; 76(1):73–82. DOI: 10.1158/0008-5472.CAN-15-1707 [PubMed: 26573799]
37. Shen T, Zhou L, Shen H, Shi C, Jia S, Ding GP, et al. Prognostic value of programmed cell death protein 1 expression on CD8+ T lymphocytes in pancreatic cancer. Sci Rep. 2017; 7(1):7848.doi: 10.1038/s41598-017-08479-9 [PubMed: 28798308]
38. Borowsky AD, Namba R, Young LJ, Hunter KW, Hodgson JG, Tepper CG, et al. Syngeneic mouse mammary carcinoma cell lines: two closely related cell lines with divergent metastatic behavior. Clin Exp Metastas. 2005; 22(1):47–59. DOI: 10.1007/s10585-005-2908-5
39. Dong H, Dube N, Shu JY, Seo JW, Mahakian LM, Ferrara KW, et al. Long-circulating 15 nm micelles based on amphiphilic 3-helix peptide-PEG conjugates. ACS Nano. 2012; 6(6):5320–9. DOI: 10.1021/nn301142r [PubMed: 22545944]
40. Cardiff RD, Hubbard NE, Engelberg JA, Munn RJ, Miller CH, Walls JE, et al. Quantitation of fixative-induced morphologic and antigenic variation in mouse and human breast cancers. Lab Invest. 2013; 93(4):480–97. DOI: 10.1038/labinvest.2013.10 [PubMed: 23399853]
41. Miller JK, Shattuck DL, Ingalla EQ, Yen L, Borowsky AD, Young LJ, et al. Suppression of the negative regulator LRIG1 contributes to ErbB2 overexpression in breast cancer. Cancer Res. 2008; 68(20):8286–94. DOI: 10.1158/0008-5472.CAN-07-6316 [PubMed: 18922900]
42. Chavez MSM, Ingham ES, Fite BZ, Mahakian LM, Tam SM, Ilovitsh A, Monjazeb AM, Murphy WJ, Hubbard NE, Davis RR, Tepper CG, Borowsky AD, Ferrara KW. Distinct immune signatures in directly treated and distant tumors result from TLR adjuvants and focal ablation. Theranostics. 2018; 8(13):3611–28. DOI: 10.7150/thno.25613 [PubMed: 30026870]
43. Silvestrini M, Ingham ES, Mahakian LM, Kheirolomoom A, Liu Y, Fite BZ, Tam SM, Tucci S, Watson KD, Wong A, Monjazeb AM, Hubbard NE, Murphy WJ, Borowsky AD, Ferrara KW. Priming is key to effective incorporation of image-guided thermal ablation into immunotherapy protocols. Jci Insight. 2017; 2(6):e90521. [PubMed: 28352658]

44. Bhat P, Leggatt G, Waterhouse N, Frazer IH. Interferon-γ derived from cytotoxic lymphocytes directly enhances their motility and cytotoxicity. Cell Death & Disease. 2017; 8:e2836.doi: 10.1038/cddis.2017.67 [PubMed: 28569770]
45. Larimer BM, Wehrenberg-Klee E, Dubois F, Mehta A, Kalomeris T, Flaherty K, et al. Granzyme B PET Imaging as a Predictive Biomarker of Immunotherapy Response. Cancer Research. 2017; 77(9):2318–27. DOI: 10.1158/0008-5472.can-16-3346 [PubMed: 28461564]
46. Walrand S, Hesse M, Jamar F. Update on novel trends in PET/CT technology and its clinical applications. The British Journal of Radiology. 2018; 91(1081):20160534.doi: 10.1259/bjr.20160534 [PubMed: 27730823]
47. Cherry SR, Jones T, Karp JS, Qi J, Moses WW, Badawi RD. Total-Body PET: Maximizing Sensitivity to Create New Opportunities for Clinical Research and Patient Care. Journal of Nuclear Medicine. 2018; 59(1):3–12. DOI: 10.2967/jnumed.116.184028 [PubMed: 28935835]
48. Pinchuk LM, Filipov NM. Differential effects of age on circulating and splenic leukocyte populations in C57BL/6 and BALB/c male mice. Immun Ageing. 2008; 5:1.doi: 10.1186/1742-4933-5-1 [PubMed: 18267021]
49. Mowat AM, Agace WW. Regional specialization within the intestinal immune system. Nat Rev Immunol. 2014; 14(10):667–85. DOI: 10.1038/nri3738 [PubMed: 25234148]
50. Tauschmann M, Prietl B, Treiber G, Gorkiewicz G, Kump P, Hogenauer C, et al. Distribution of CD4(pos) -, CD8(pos) - and regulatory T cells in the upper and lower gastrointestinal tract in healthy young subjects. PLoS One. 2013; 8(11):e80362.doi: 10.1371/journal.pone.0080362 [PubMed: 24265815]
51. Brimnes J, Allez M, Dotan I, Shao L, Nakazawa A, Mayer L. Defects in CD8+ regulatory T cells in the lamina propria of patients with inflammatory bowel disease. J Immunol. 2005; 174(9):5814–22. [PubMed: 15843585]
52. Funderburg NT, Stubblefield Park SR, Sung HC, Hardy G, Clagett B, Ignatz-Hoover J, et al. Circulating CD4(+) and CD8(+) T cells are activated in inflammatory bowel disease and are associated with plasma markers of inflammation. Immunology. 2013; 140(1):87–97. DOI: 10.1111/imm.12114 [PubMed: 23600521]
53. Johansson-Percival A, He B, Li ZJ, Kjellen A, Russell K, Li J, et al. De novo induction of intratumoral lymphoid structures and vessel normalization enhances immunotherapy in resistant tumors. Nat Immunol. 2017; 18(11):1207–17. DOI: 10.1038/ni.3836 [PubMed: 28892469]
54. Pfirschke C, Engblom C, Rickelt S, Cortez-Retamozo V, Garris C, Pucci F, et al. Immunogenic Chemotherapy Sensitizes Tumors to Checkpoint Blockade Therapy. Immunity. 2016; 44(2):343–54. DOI: 10.1016/j.immuni.2015.11.024 [PubMed: 26872698]
55. Smyth MJ, Ngiow SF, Ribas A, Teng MW. Combination cancer immunotherapies tailored to the tumour microenvironment. Nat Rev Clin Oncol. 2016; 13(3):143–58. DOI: 10.1038/nrclinonc.2015.209 [PubMed: 26598942]
56. Kang J, Demaria S, Formenti S. Current clinical trials testing the combination of immunotherapy with radiotherapy. J Immunother Cancer. 2016; 4:51.doi: 10.1186/s40425-016-0156-7 [PubMed: 27660705]
57. Weichselbaum RR, Liang H, Deng L, Fu YX. Radiotherapy and immunotherapy: a beneficial liaison? Nat Rev Clin Oncol. 2017; 14(6):365–79. DOI: 10.1038/nrclinonc.2016.211 [PubMed: 28094262]
58. Davila E, Velez MG, Heppelmann CJ, Celis E. Creating space: an antigen-independent, CpG-induced peripheral expansion of naive and memory T lymphocytes in a full T-cell compartment. Blood. 2002; 100(7):2537–45. DOI: 10.1182/blood-2002-02-0401 [PubMed: 12239167]
59. Klinman DM. Immunotherapeutic uses of CpG oligodeoxynucleotides. Nat Rev Immunol. 2004; 4(4):249–58. DOI: 10.1038/nri1329 [PubMed: 15057783]
60. Selby MJ, Engelhardt JJ, Johnston RJ, Lu LS, Han M, Thudium K, et al. Correction: Preclinical Development of Ipilimumab and Nivolumab Combination Immunotherapy: Mouse Tumor Models, In Vitro Functional Studies, and Cynomolgus Macaque Toxicology. PLoS One. 2016; 11(11):e0167251.doi: 10.1371/journal.pone.0167251 [PubMed: 27861630]

61. Tumeh PC, Harview CL, Yearley JH, Shintaku IP, Taylor EJ, Robert L, et al. PD-1 blockade induces responses by inhibiting adaptive immune resistance. Nature. 2014; 515(7528):568–71. DOI: 10.1038/nature13954 [PubMed: 25428505]

62. Liu D, Cao G, Cen Y, Liu T, Peng W, Sun J, et al. The radiosensitizing effect of CpG ODN107 on human glioma cells is tightly related to its antiangiogenic activity via suppression of HIF-1alpha/VEGF pathway. Int Immunopharmacol. 2013; 17(2):237–44. DOI: 10.1016/j.intimp.2013.06.002 [PubMed: 23791618]

63. Wu J, Su W, Powner MB, Liu J, Copland DA, Fruttiger M, et al. Pleiotropic action of CpG-ODN on endothelium and macrophages attenuates angiogenesis through distinct pathways. Sci Rep. 2016; 6:31873.doi: 10.1038/srep31873 [PubMed: 27558877]

64. Heikenwalder M, Polymenidou M, Junt T, Sigurdson C, Wagner H, Akira S, et al. Lymphoid follicle destruction and immunosuppression after repeated CpG oligodeoxynucleotide administration. Nat Med. 2004; 10(2):187–92. DOI: 10.1038/nm987 [PubMed: 14745443]

Translational Relevance

Non-invasive molecular imaging techniques such as PET can provide the required specificity to distinguish immune system components in living organisms over the course of disease development, progression, and treatment. In this study, an anti-CD8 cys-diabody was labeled with ^{64}Cu and used to study tissue-specific differences in immune cell density between mouse strains, within each mouse, and with response to treatment. The study presented here shows that immunoPET can be applied to map CD8^{+} T-cell density and suggests that this technique can be applied to a range of basic science and translational therapeutic applications. With the rapid proliferation of immune therapeutic strategies, such imaging techniques can play a key role in the design and evaluation of treatment protocols. Importantly, we detect dramatic changes in the liver, spleen and tumor, demonstrating the importance of systemic, non-invasive imaging of efficacy and a potential role in evaluating side effects and toxicity. Most importantly, this new imaging probe facilitates serial imaging of T-cell distribution over the course of treatment.

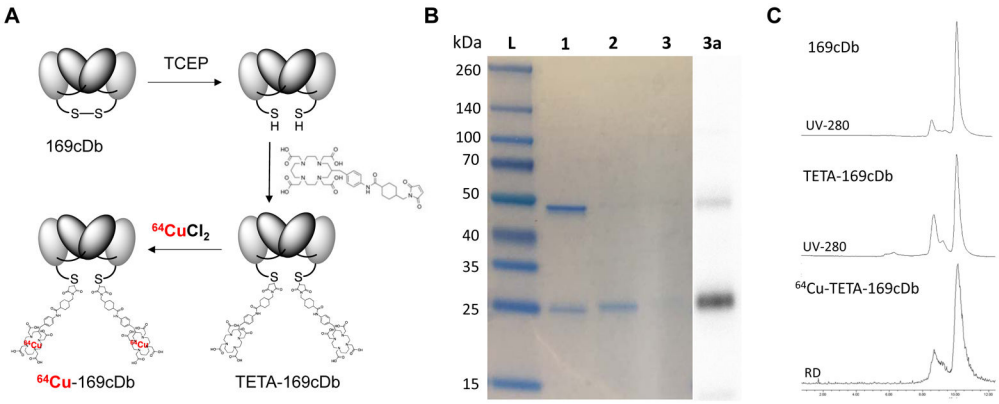

Fig. 1.

Characterization of ^{64}Cu-169cDb and intermediates. (*A*) Scheme of ^{64}Cu-labeling of 169cDb. TETA-maleimide was site-specifically conjugated to reduced thiol on 169cDb. Isolated TETA-169cDb was labeled with ^{64}Cu in 0.1 M ammonium citrate (pH 7.4). (*B*) SDS-PAGE gel electrophoresis of cys-diabodies (**L**: Ladder, **1**: 169cDb, **2**:TETA-169cDb, **3**: ^{64}Cu-169cDb, **3a**: autoradiography of ^{64}Cu-169cDb. (*C*) Size exclusion chromatograms of 169cDb (top, 280 nm UV), TETA-169cDb (middle, 280 nm UV), and ^{64}Cu-TETA-169cDb (bottom, radiodetector).

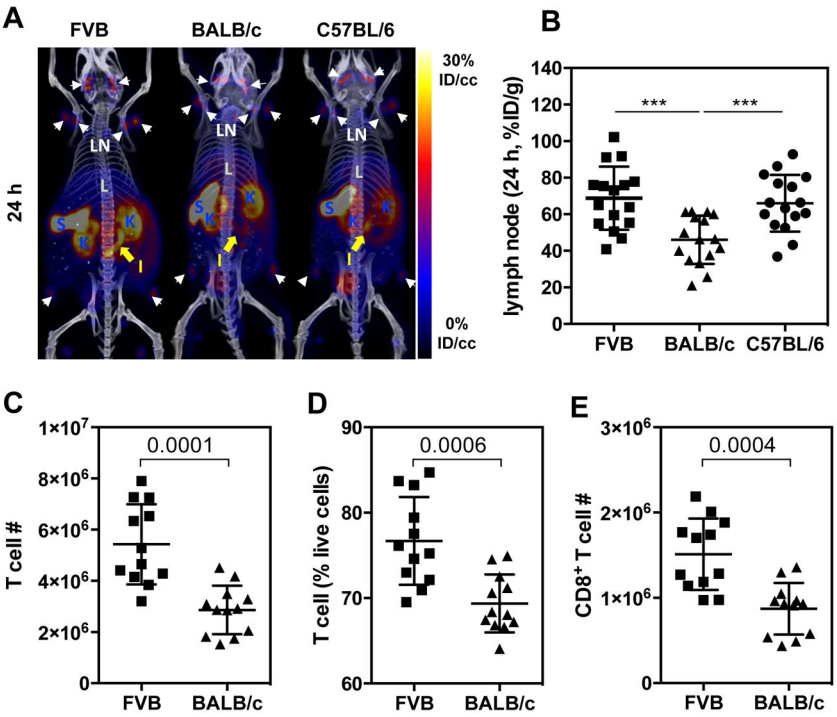

Fig. 2.

PET/CT image, image-derived accumulation of ^{64}Cu-169cDb and results of validation by flow cytometry, each in wild-type mice. (*A*) Projected small animal PET/CT images of wild-type FVB (left), BALB/c (middle), and C57BL/6 (right) mouse acquired at 24 hours after intravenous administration of ^{64}Cu-TETA-169cDb (3.7 ± 0.30 mg) through the tail vein. (LN: Lymph Node (white arrows), S: Spleen, K: Kidney, L: Liver, and I: intestine (yellow arrow)). Image intensity is scaled as the maximum 30% ID/cc. (*B*) Biodistribution of ^{64}Cu-169cDb (%ID/g), measured at 24 hours, in pooled lymph nodes (axillary, inguinal, cervical and mesenteric) from wild-type FVB (n=4, left), BALB/c (n=4, middle), and C57BL/6 (n=4, right) mice. (C)-(E) Results from flow cytometry of pooled lymph nodes harvested from FVB (n=4) and BALB/c (n=4) mice. Each data point represents two pooled axillary, inguinal, or cervical lymph nodes from each mouse (Method S3). (C) The number of T-cells ($CD45^+CD3^+$ cells), (D) the fraction of T-cells ($CD45^+CD3^+$ cells given as a percentage of live cells) and (E) the number of $CD8^+$ T cells. Data, mean ± SD (unpaired t test with Welch's correction, *** $P < 0.001$ in (B), exact numerical P values are given in (C–E)).

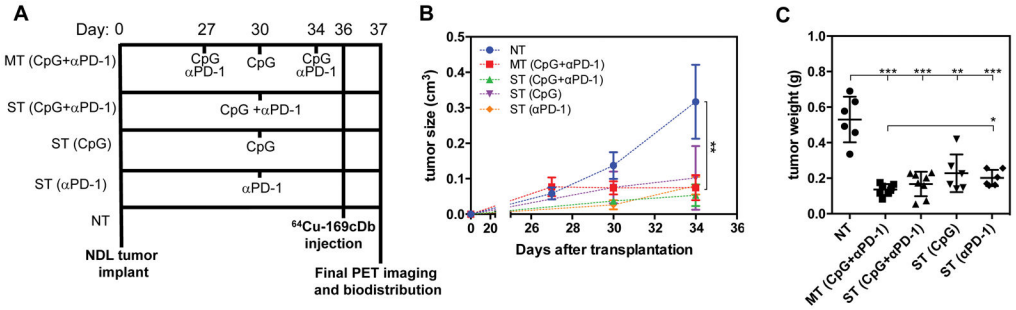

Fig. 3.

Cancer immunotherapy protocols and resulting efficacy. (*A*) Immunotherapy and immunoPET/CT imaging scheme for FVB mice bearing bilateral orthotopic syngeneic NDL tumors in the fourth and ninth mammary fat pads. CpG was directly injected into the right or left tumor and anti-PD-1 (αPD-1) was intraperitoneally administered. (NT: non-treatment, MT: multiple treatment, ST: single treatment) (*B*) Tumor volume (cm^3) over time. Tumor volume measured on the day of drug treatment is found in Supplementary Table S4. On day 34, the tumor volume of each treated group was smaller than that of no-treated group (unpaired t test with Welch's correction, **, $P < 0.01$). (*C*) Tumor weight (gram) measured at day 37 after tumor implant (Table S5). NT (n=3, n_{tumor}=6), MT (CpG+αPD-1, n=4, n_{tumor}=8), ST (CpG+αPD-1, n=4, n_{tumor}=8), ST (CpG, n=3, n_{tumor}=6), and ST (αPD-1, n=3, n_{tumor}=6). Data, mean ± SD (unpaired t test with Welch's correction, *, $P < 0.05$; **, $P < 0.01$; *** $P < 0.001$).

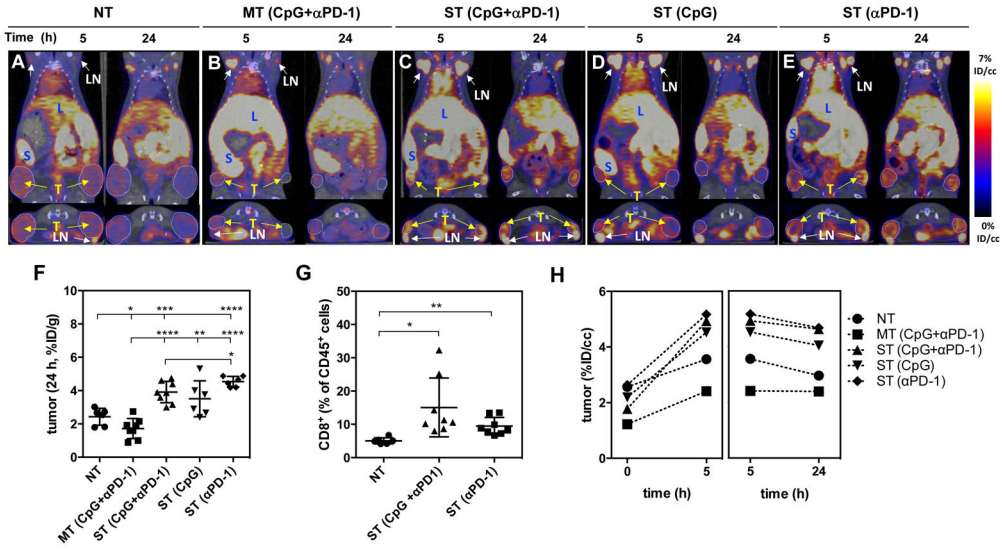

Fig. 4.

PET/CT slice images and image-derived ^{64}Cu-169cDb accumulation in the NDL tumor model following treatment protocols shown in Fig. 3. (*A*–*E*) Sliced coronal (upper) and transverse (lower) PET/CT images from (*A*) NT, (*B*) MT (CpG+αPD-1), (*C*) ST (CpG+αPD-1), (*D*) ST (CpG), and (*E*) ST (αPD-1) mice, acquired at 5 (left) and 24 (right) hours after IV administration of ^{64}Cu-169cDb. Maximum intensity was set to 7 %ID/g. Tumors are circled. Yellow and white arrows indicate tumor and lymph nodes, respectively. (L: liver, S: spleen, and K: kidneys) (*F*) Biodistribution of ^{64}Cu-169cDb in tumor (%ID/g) at 24 hours after IV administration. NT (n=3, n_{tumor}=6), MT (CpG+αPD-1, n=4, n_{tumor}=8), ST (CpG+αPD-1, n=4, n_{tumor}=8), ST (CpG, n=3, n_{tumor}=6), and ST (αPD-1, n=3, n_{tumor}=6). Data, mean ± SD (unpaired t test with Welch's correction, *, $P < 0.05$; **, $P < 0.01$; ***, $P < 0.001$; **** $P < 0.001$) (*G*) Flow cytometry quantification of the fraction of $CD45^+CD8^+$ T-cells in NDL tumors harvested 7 days after ST (CpG+aPD-1, n=4), ST (αPD-1, n=4) and NT (n=3) (Method S3). Data, mean ± SD (unpaired t test with Welch's correction, *, $P < 0.05$; **, $P < 0.01$) (*H*) Radioactivity (%ID/cc) in tumor ROI over 24 hours (Further detailed in Supplementary Table S8).

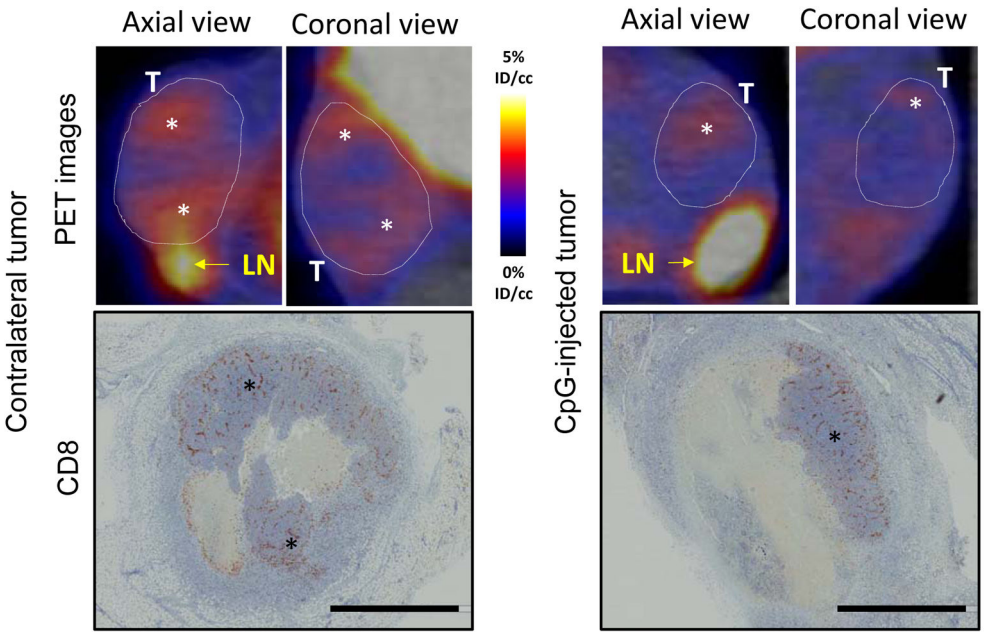

Fig. 5.

Images from PET/CT (top) and CD8a immunohistochemistry (IHC) (bottom) of NDL tumors from mice receiving multiple treatments with CpG+αPD-1 as described in Fig. 3. Tumors are circled in PET images and the asterisks in PET and IHC images represent regions of viable tumor with infiltrating $CD8^+$ T-cells (brown color). T (white) and LN (yellow) indicate tumor and lymph nodes, respectively (image scale: black bar, 2 mm). Maximum intensity was set to 5 %ID/g.

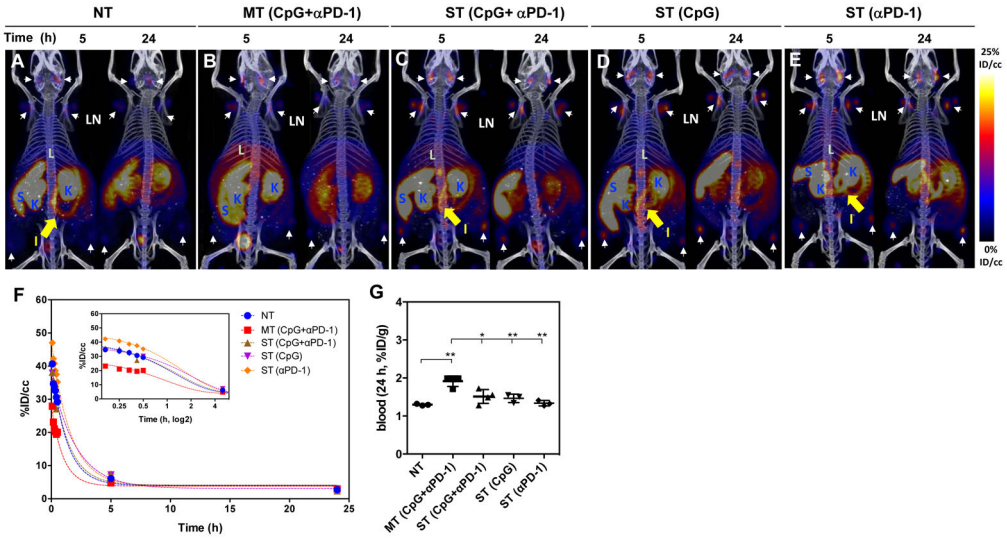

Fig. 6.

Projected PET/CT images and image-based diabody concentration in blood of NDL-tumor mice treated based on protocol in Fig. 3. (*A*–*E*) Projected PET/CT images from (*A*) NT, (*B*) MT (CpG+αPD-1), (*C*) ST (CpG+αPD-1), (*D*) ST (CpG), and (*E*) ST (αPD-1) mice, acquired at 5 (left) and 24 (right) hours after IV administration of ^{64}Cu-169 cDb. White and yellow arrows indicate lymph nodes and intestine, respectively. L: liver, S: spleen, and K: kidneys. Maximum intensity was set to be 25 %ID/g. (*F*) Time activity curve (%ID/cc) of blood obtained from ROI of left ventricle of tumor-bearing mice receiving the same treatments as in (*A*–*E*). First 30 minute images were segmented as 6 frames (5 min/frame) and time points were fitted as one-phase decay curve (Y=(Y0 − Plateau)*exp(−K*X) + Plateau). The inset graph in (*F*) represents the same time activity curve in log scale up to 5 hours. (*G*) Radioactivity of blood (%ID/g) measured in well by gamma counter at 24 h after IV administration of ^{64}Cu-169cDb. NT (n=3), MT (CpG+αPD-1, n=4), ST (CpG+αPD-1, n=4), ST (CpG, n=3), and ST (αPD-1, n=3). Data, mean ± SD (unpaired t test with Welch's correction, *, $P < 0.05$; **, $P < 0.01$).